Journal of Asian Earth Sciences 239 (2022) 105418

Contents lists available at ScienceDirect

Journal of Asian Earth Sciences

journal homepage: www.elsevier.com/locate/jseaes

An aeromagnetic study of fault structures underneath the region across the Chinese Altai orogen, Junggar Basin, Tianshan orogen, and Tarim Basin

Xiaosan Zhu *, Tao Wang, He Huang, Hongwei Zheng

Institute of Geology, Chinese Academy of Geological Sciences, Beijing 100037, PR China

ARTICLE INFO

Keywords:
Aeromagnetic data
Magnetic anomaly
Magnetic susceptibility
Crustal structure
Central Asian Orogenic Belt

ABSTRACT

In this study, an aeromagnetic dataset is used to investigate the crustal structure in the region across the Chinese Altai orogen, Junggar Basin, Tianshan orogen, and Northern Tarim Basin, providing insights into the unclear nature of the basement of the Junggar Basin. The aeromagnetic data are for a region containing the Chinese Altai, Junggar Basin, Tianshan Mountains, and Tarim Basin. On the basis of magnetic anomalies, we identify several faults and volcanic suites in this region. According to the magnetic characteristics, gravity anomalies, and crustal thickness, we suggest that the Junggar Basin has a basement composed of oceanic crustal material or continental-like material. Mantle upwelling occurred in the West Junggar orogenic belt during the Late Carboniferous–Cretaceous. The faults we have identified provide useful insights into the tectonic development in the northwestern Central Asian Orogenic Belt.

1. Introduction

The Central Asian Orogenic Belt (CAOB) (Windley et al., 1990, 2007; Jahn et al., 2000; Xiao and Santosh, 2014; Wang et al., 2004, 2017), which is also known as the Altaids (Şengör et al., 1993) and the Central Asian fold belt (Zonenshain et al., 1990; Buchko et al., 2008; Sorokin et al., 2010), is one of the world's largest accretionary orogens and is bordered by the Siberian Craton to the north and the Tarim and Sino-Korean cratons to the south (Fig. 1). This orogen was mainly formed by the subduction and accretion of juvenile material during the Neoproterozoic and Paleozoic (Fig. 1) (Windley et al., 1990, 2007; Xiao et al., 2008, 2009, 2015a, 2015b, 2019; Xiao and Santosh, 2014; Han and Zhao, 2018). Subduction–accretionary complexes, arc magmatic rocks, and arc-associated basins occur in the orogen (Şengör and Natal'in, 1996; Xiao and Santosh, 2014; Gao et al., 2018; Xiao et al., 2018).

Many studies have investigated the tectonic units and the compositions of the accretionary complexes in the CAOB and its various constituent parts. Li (1985, 1986) examined the tectonic units of the northern Xinjiang and Greater Khingan Mountains–Mongolia regions with respect to the subduction-collision of the three major plates involved in the development of the CAOB. Several studies have investigated the deep structure and compositions of the geological bodies in the tectonic domains in the CAOB (Gao et al., 2002; Zhao et al., 2004; Wang et al., 2004, 2020; Yang et al., 2015a, 2015b; Jiang et al., 2016; Xu et al., 2016; Wu et al., 2018; Li et al., 2019; Guy et al., 2020). For example, the deep structures in regions such as the Chinese Altai, Junggar Basin, Tianshan Mountains, and Tarim Basin have been studied using seismic reflection data, broadband seismic data, and wide-angle reflection and deep seismic reflection sounding data (Gao et al., 2002; Wang et al., 2004, 2020;Wu et al., 2018; Li et al., 2019; Yang et al., 2022). Deep exploration of the Chinese Altai, eastern Junggar Basin, and Korla–Jimusar area has been conducted using gravity and magnetic data (Zhao et al., 2004; Jiang et al., 2016; Guy et al., 2020; Zheng et al., 2021). Li et al. (2006) obtained the S-wave velocity structure of the crust and upper mantle of the Tianshan orogenic belt. Guy et al. (2020) found a dense lower crust in the East Junggar region. Wu et al. (2018) determined the Moho variations along three NW-SE profiles in the Junggar Basin based on seismic data. Zhao et al. (2004) and Wang et al. (2004) identified low-density bodies at the top of the upper mantle at the junction between the Junggar Basin and the Tianshan orogenic belt, as well as at the junction between the Tarim Basin and the Tianshan orogenic belt. Zhang et al. (2021) identified the trench-arc-basin system in the West Junggar region. Yang et al. (2022) determined that two trapped oceanic basins form parts of the low crust in the southern Altaids. Magnetotelluric (MT) data have been used to detect the distribution and characteristics of the resistivity of the northwestern Chinese Altai, Junggar Basin, Tianshan, and Tarim Basin (Yang et al., 2015a, 2015b; Xu et al., 2016). Xu et al. (2016) discovered a Late Carboniferous

* Corresponding author at: No. 26 Baiwanzhuang Road, Xicheng District, Beijing 100037, PR China.
E-mail address: zhuxiaosan129@outlook.com (X. Zhu).

https://doi.org/10.1016/j.jseaes.2022.105418
Received 27 July 2022; Received in revised form 16 September 2022; Accepted 19 September 2022
Available online 24 September 2022
1367-9120/© 2022 Published by Elsevier Ltd.

intra-oceanic subduction system with a SE to NW subduction direction in the western Junggar Basin. Yang et al. (2015a, 2015b) studied the three-dimensional lithospheric structure of the Tarim terrane based on its electrical structural features. Despite these previous studies, further investigations are required in various regions of the CAOB to better constrain their tectonic, structural, and geological characteristics and to infer the evolution of these regions and the entire CAOB.

The Junggar Basin and the surrounding areas, i.e., the Chinese Altai, Tianshan Mountains, and Tarim Basin, are ideal locations for studying the tectonic evolution of the CAOB. Various proposals have been put forward regarding the basement properties and deep sutures of the Junggar Basin. Several previous studies have suggested that Precambrian crystalline basement is present in the basin (Ren, 1984; Wang, 1986; Wu, 1986), whereas others have suggested the presence of Paleozoic oceanic crustal material (Jiang, 1984; Coleman, 1989; Feng et al., 1989; Xu et al., 2020). In addition, there are different opinions regarding the tectonic setting during the Late Paleozoic and the pattern of the oceanic plate subduction. Several studies have suggested that the Late Paleozoic tectonic setting of the West Junggar region was a series of continental arcs (Zhang and Huang, 1992) or subduction systems associated with oceanic arcs (Jiang, 1984; Li, 1985, 1986; Coleman, 1989; Feng et al., 1989; Su et al., 2006; Xiao et al., 2008). The proposed models of oceanic plate subduction include northwestward subduction (Li et al., 2006), double-sided subduction (Yang et al., 2012), northwestward intraoceanic subduction (Xu et al., 2016; Wu et al., 2018), and subduction of ocean ridges (Geng et al., 2009). As these processes should be

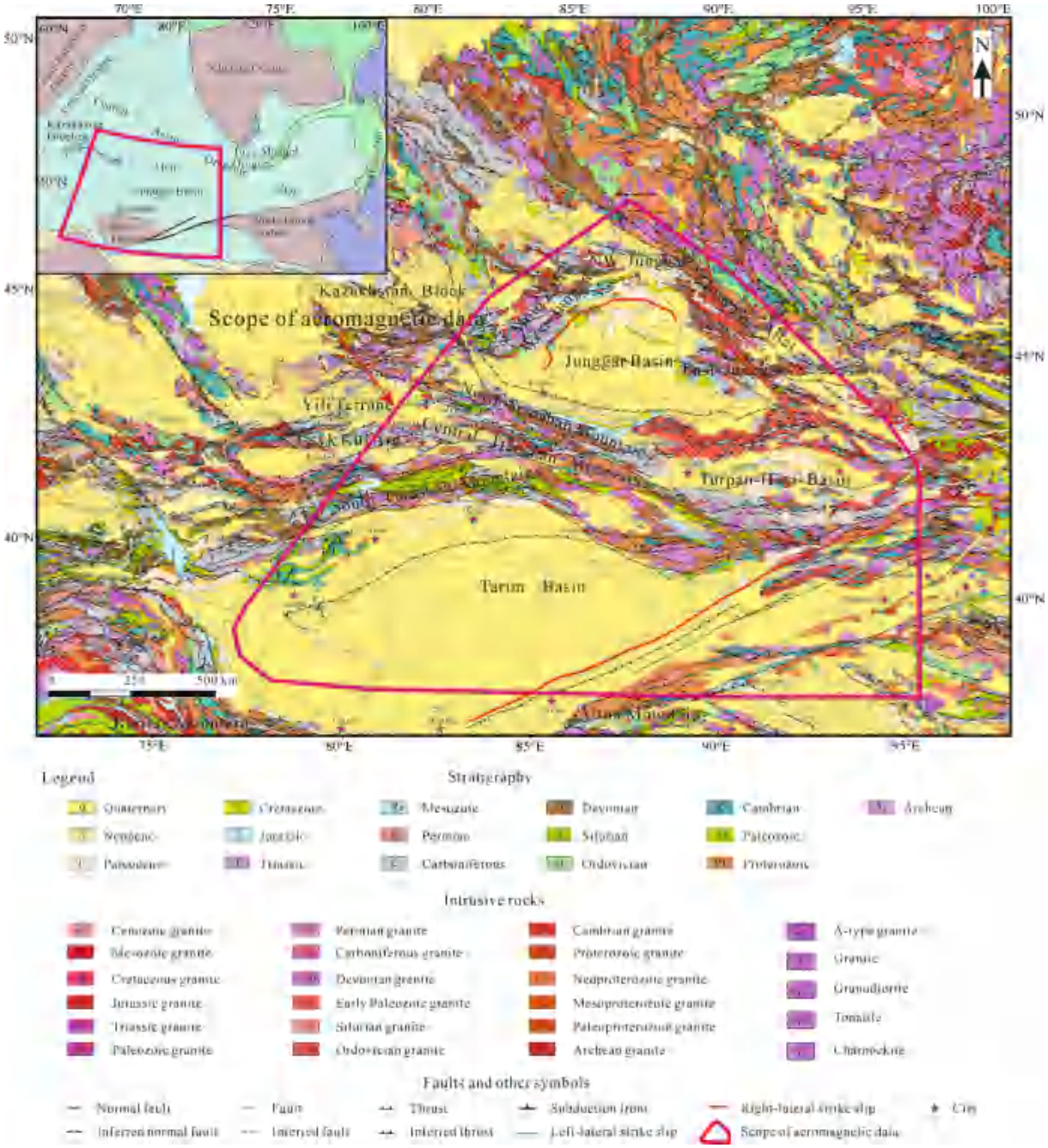

Fig. 1. Simplified geological map of the Chinese Altai, Junggar Basin, Tianshan Mountains, and Tarim Basin regions showing the extent of the study area (outlined in red) (modified after Ren, 2015; Chen et al., 2017; Wang et al., 2017). The latitude and longitude ranges of the area of magnetic data acquisition are 38.4–48.6°N and 75.4–96.1°E, respectively. (For interpretation of the references to colour in this figure legend, the reader is referred to the web version of this article.)

recorded in the crustal structures of both the Junggar Basin and the West Junggar region, it is necessary to conduct deep structural studies in these regions to clarify the tectonic evolution of this part of the CAOB. However, a full geophysical characterization of the crustal structures of the northwestern CAOB and of the nature of the basement of the Junggar Basin has not been conducted.

2. Geological setting

The northwestern CAOB consists of the Altai, Junggar and Tianshan Mountains tectonic units (Xiao et al., 2008, 2009, 2010, 2013, 2015a, 2015b; Xiao and Santosh, 2014) from north to south. The Chinese Altai orogen consists of various juvenile tectonic units, including fragments of island arcs (Alaskan-type), oceanic islands, seamounts, ophiolites, gneissic massifs, and accretionary complexes (Xiao et al., 2010). Together, these units comprise an Early Paleozoic juvenile magmatic arc terrane that developed on the Neoproterozoic continental margin of the Tuva-Mongol microcontinent (Sun et al., 2008; Long et al., 2010; Li et al., 2016, 2021).

The Junggar area, including West Junggar, East Junggar, and the Junggar Basin, consists of Paleozoic continental margin sequences and volcanic, ophiolitic, sedimentary, and intrusive rocks (Xiao et al., 2013; Gao et al., 2018). This area has undergone a complex evolution, including Paleozoic subduction and collision and Mesozoic thrusting, uplift, and erosion related to the formation of the Tianshan Mountains (Windley et al., 1990; Xiao et al., 2008; Li et al., 2015). The Junggar Basin has been in a tectonically stable intracontinental stage of evolution since the Mesozoic, during which numerous intermontane basins have developed (Su et al., 2006).

Three main stages of intrusive rocks formed in West Junggar (Zhang et al., 2021). The first stage consisted of Late Silurian–Early Devonian (436–405 Ma) intrusive rocks, including alkali-feldspar granite, granodiorite, quartz diorite, and monzonite diorite, which are distributed in the Seamistai Mountains. The second stage consisted of Early Carboniferous granites (mainly alkali-feldspar granite and monzonite granite; 345–321 Ma). These granites are mainly located in the Hatu and Tiechanggou areas and intruded into the Middle–Upper Devonian neritic-littoral pyroclastic rock and clastic rock formations, which in turn are covered by Jurassic–Triassic strata (Zhang et al., 2021). The third stage consisted of widely distributed Late Carboniferous–Early Permian intrusions that are primarily composed of alkali granite, monzonite granite, and granodiorite (318–290 Ma) which intruded into Carboniferous clastic rocks (Zhang et al., 2021).

West Junggar was influenced by intraoceanic subduction and accretion during the Paleozoic, resulting in the formation of several ophiolitic mélange belts and paleocontinental–margin–accretion systems (Zhang and Huang, 1992). The Tangbale, Mayil, Barrek, Maria, Dalbut, and Baijiantan ophiolite mélanges have been identified in this region, as well as the Karamay, Dagun, and Hatu structural mélanges (Guy et al., 2020).

The Tianshan Mountains were the site of the accretion of several island arcs and the collision of continental blocks during the Paleozoic; large-scale dextral strike-slip faulting during the Permian; and rejuvenation as an intracontinental orogen during the Cenozoic collision between the Indian and Eurasian plates (Molnar and Tapponnier, 1975; Tapponnier and Molnar, 1979; Windley et al., 1990; Xiao et al., 2013). The Tianshan Mountains are traditionally subdivided from north to south into the North, Central, and South Tianshan Mountains.

The igneous rocks in the Tianshan Mountains are distributed in various tectonic units and regions, are composed of complex lithological types (mainly marine volcanic rocks), and were mostly formed during the Carboniferous (Ji et al., 1999; Guo et al., 2002; Wang et al., 2007; Yu et al., 2016). Of the Paleozoic igneous rocks, andesites are the most widely distributed, followed by basalts, with subordinate dacites and rhyolites, as well as minor ultramafic rocks and alkaline igneous rocks. The Proterozoic igneous rocks are distributed mainly in the Borokonu and East Junggar areas, with minor amounts in the Kuruk-tagh region (Liu et al., 2017), and they consist mainly of metamorphosed basalt and andesite, as well as some rhyolite.

3. Magnetic susceptibility of rock samples from the NW CAOB

Magnetic susceptibility is defined as the ratio of the rock's magnetization to the magnetic field strength, which is an intrinsic property of rocks (and orebodies). The magnetic susceptibilities of rocks are related to their chemical composition and structure and more specifically to the content of ferromagnetic materials (Baranov, 1957; Baranov and Naudy, 1964).

The magnetic susceptibility data for rock samples acquired from the Junggar Basin, Tianshan Mountains, and adjacent areas were measured at the China University of Geosciences (Wuhan) (Table 1). Generally, ferromagnetic minerals, such as those in diabase, basalt, gabbro, mafic lava, serpentine, and chrome ore, can cause strong magnetic anomalies. Of these minerals, magnetite has the strongest magnetic properties, resulting in strong magnetic anomalies and a gradient with a large spatial variation. Most igneous rocks have markedly greater susceptibility values, including rocks such as monzonite granite, diorite, granite, syenite porphyry, K-feldspar granite, diorite, and pyrite. Mafic intrusive rocks have strong magnetic susceptibilities, and the felsic rocks have relatively weak magnetic susceptibilities. The magnetic properties of intrusive rocks increase gradually from felsic to mafic compositions, and those of igneous rocks of the same lithology vary from deep to shallow intrusives and to erupted rocks. Sedimentary rocks typically have either no or weak susceptibility, including rocks such as sandstone, siltstone, feldspar–quartz sandstone, siliceous rock, and mudstone (Zheng et al., 2021).

Generally, magnetite and other ferromagnetic minerals have the strongest magnetic properties, followed by igneous rocks. Sedimentary

Table 1
Magnetic susceptibilities of rock and ore samples from the Junggar Basin, Tianshan Mountains, and adjacent areas.

Sample number	Lithology	Number of samples	Magnetic susceptibility ($\times 10^{-6}$ SI)	
			Range	Mean
1	Mudstone	31	25–752	152
2	Medium-grained sandstone	7	77–723	235
3	Siliceous rock	108	145–18,200	304
4	Feldspar–quartz sandstone	12	33–431	334
5	Feldspar lithic sandstone	57	99–577	371
6	Tuffaceous fine sandstone	3	452–540	496
7	Tuffaceous siltstone	189	640–10,880	609
8	Siltstone	1011	19–63,490	688
9	Sandstone	14	60–4325	757
10	Andesite	4	407–888	537
11	Andesite porphyry	3	93–1385	625
12	Pyrite	8	421–1085	665
13	Mafic lava	13	113–63,350	9836
14	Basalt	95	62–125,300	12,810
15	Granite porphyry	12	29–419	140
16	Tuff	17	160–447	347
17	Diorite porphyrite	20	90–3657	711
18	Potassium feldspar granite	162	5230–11,813	1495
19	Syenite porphyry	3	1594–1786	1700
20	Granite	752	8–51,470	2100
21	Diorite	111	604–40,830	3626
22	Monzonite granite	71	22–29,010	5174
23	Gabbro	24	59–76,050	8331
24	Diabase	82	63–87,470	10,272
25	Serpentine	68	77.9–131,750	38,471
26	Chrome ore	14	1250–68,630	30,672

rocks have the weakest magnetic properties. The magnetic susceptibilities of the same rock type increase as the content of mafic minerals increases. Rocks derived from crustal sources tend to have low magnetic susceptibilities, those derived from mixed crust-mantle sources have intermediate susceptibilities, and those derived from mantle sources generally have high susceptibilities(Baranov, 1957; Baranov and Naudy, 1964; Zheng et al., 2021).

4. Data collection, processing, and inversion

The aeromagnetic data used in this study were acquired by the China Geological Survey between 2010 and 2015 and are presented at a scale of 1:100,000 (Fig. 2). The average interval of the flying lines is ~5 km. The latitude and longitude ranges of the area of data acquisition are 38.4–48.6°N and 75.4–96.1°E, respectively.

Several processing procedures were used to suppress the noise, extract and strengthen the useful information, and enhance the geological interpretability of the magnetic ΔT anomalies (Baranov, 1957; Zhu and Lu, 2016, 2021; Zhu et al., 2018, 2019, 2022) (Fig. 2). The locations, distributions, and regional extents of magnetic anomalies can be defined through magnetic data processing (Clark, 2014; Biedermann and McEnroe, 2017). Similarly, faults and volcanic units at different depths can be identified and interpreted after data processing (Clark, 1997). In this study, we conducted reduction to pole (RTP) (Fig. 3), upward continuation, derivative calculations in the vertical direction (Fig. 4), boundary enhancement (Figs. 5–6), and analytical signal amplitude procedures (Fig. 7) using the Modelvision (V14.0) software during the processing of the magnetic data (Baranov and Naudy, 1964; Kadasi, 2015; Ranganai et al., 2016). These procedures are described in detail below.

The RTP transformation of total field magnetic anomalies is intended to remove the skewness of the anomalies. The transformation makes the anomalies overlie their sources, makes it possible to correlate the magnetic anomalies with other types of geophysical anomalies and geological information, and aids in their interpretation (Baranov, 1957; Baranov and Naudy, 1964). The magnetic field parameters were chosen based on the international reference geomagnetic field (Thébault et al., 2010).

The upward continuation procedure transforms the magnetic data to make it appear as if they were collected at a greater height than was actually the case (Henderson, 1970; Jacobsen, 1987). This transformation can weaken high-frequency signals and results in low-pass filtering of the magnetic data (Henderson, 1970; Jacobsen, 1987; Zhu and Lu, 2016, 2021). In this study, we conducted an upward continuation procedure at heights of 5,000, 10,000, 20,000, 30,000, and 50,000 m (Fig. 3).

The derivatives of the magnetic anomalies were calculated to eliminate the background anomaly values of the normal field, suppress the effects of the regional field, separate superimposed anomalies, and identify anomalies caused by adjacent magnetic anomaly bodies (Zhu and Lu, 2016, 2021; Zhu et al., 2019). The zero line of the second-order derivative in the vertical direction, based on the magnetic ΔT anomaly obtained from the RTP data, can be used to identify the magnetic anomalies caused by concealed geological bodies and constrain their locations and extents (Wang et al., 2010). In this study, we calculated the second derivative in the vertical direction using the magnetic data after the RTP and upward continuation procedures at different heights (Fig. 4).

A boundary enhancement calculation procedure was used to enhance the subsurface structural information, suppress the non-structural information, and identify the positions of fractures and boundaries of magnetic bodies. This procedure can overcome both shallow and deep sources of interference and provides accurate fault locations when combined with the upward continuation procedure during data processing (Wang et al., 2009; Zhu and Lu, 2016, 2021; Zhu et al., 2019, 2022). We used the tilt derivative for the boundary enhancement calculation (Miller and Singh 1994) and calculated the boundary enhancement using the magnetic data subjected to RTP and upward continuation procedures at different heights (Figs. 5–6).

Signal amplitude analysis was conducted to establish the boundaries and centers of the magnetic anomaly bodies (Nabighian, 1972; Zhu and Lu, 2016, 2021; Zhu et al., 2019, 2022). The position of the peak signal amplitude represents the boundary of a magnetic anomaly body when the data acquisition station is close to the body, and it represents the

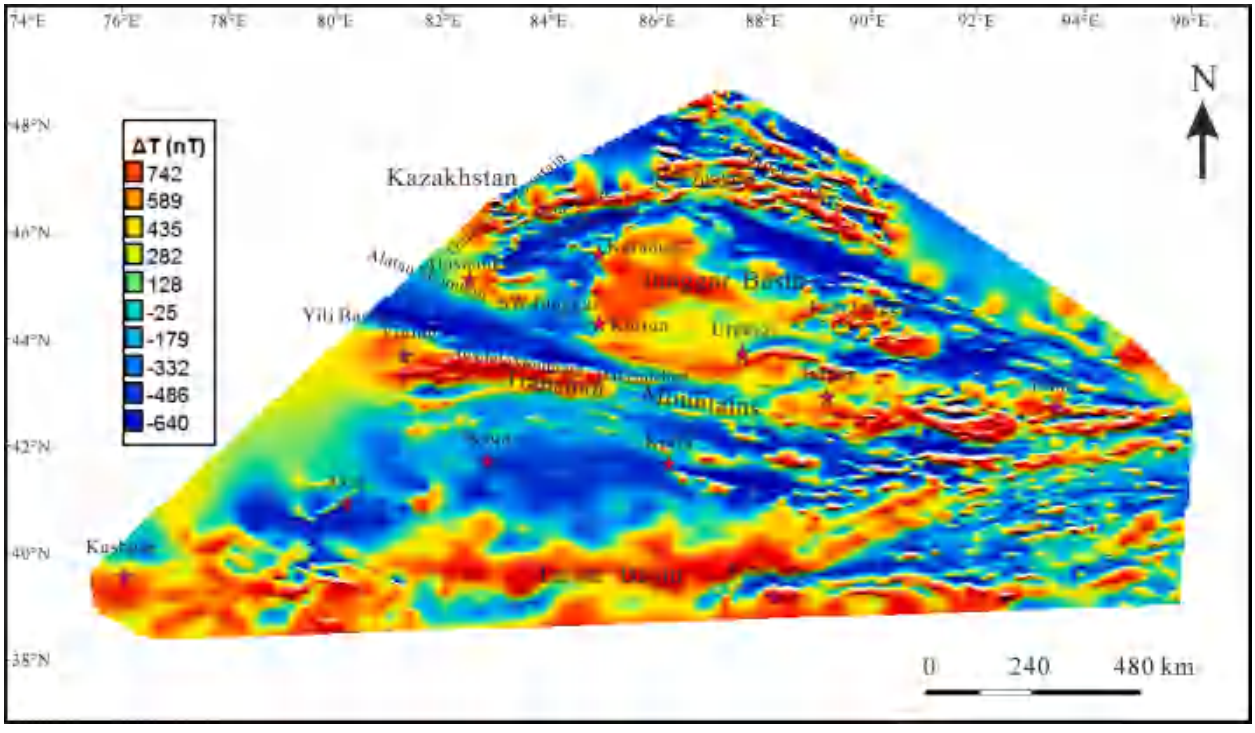

Fig. 2. Distribution of aeromagnetic ΔT anomalies in the study area, including the Chinese Altai, Junggar Basin, Tianshan Mountains, and Tarim Basin regions.

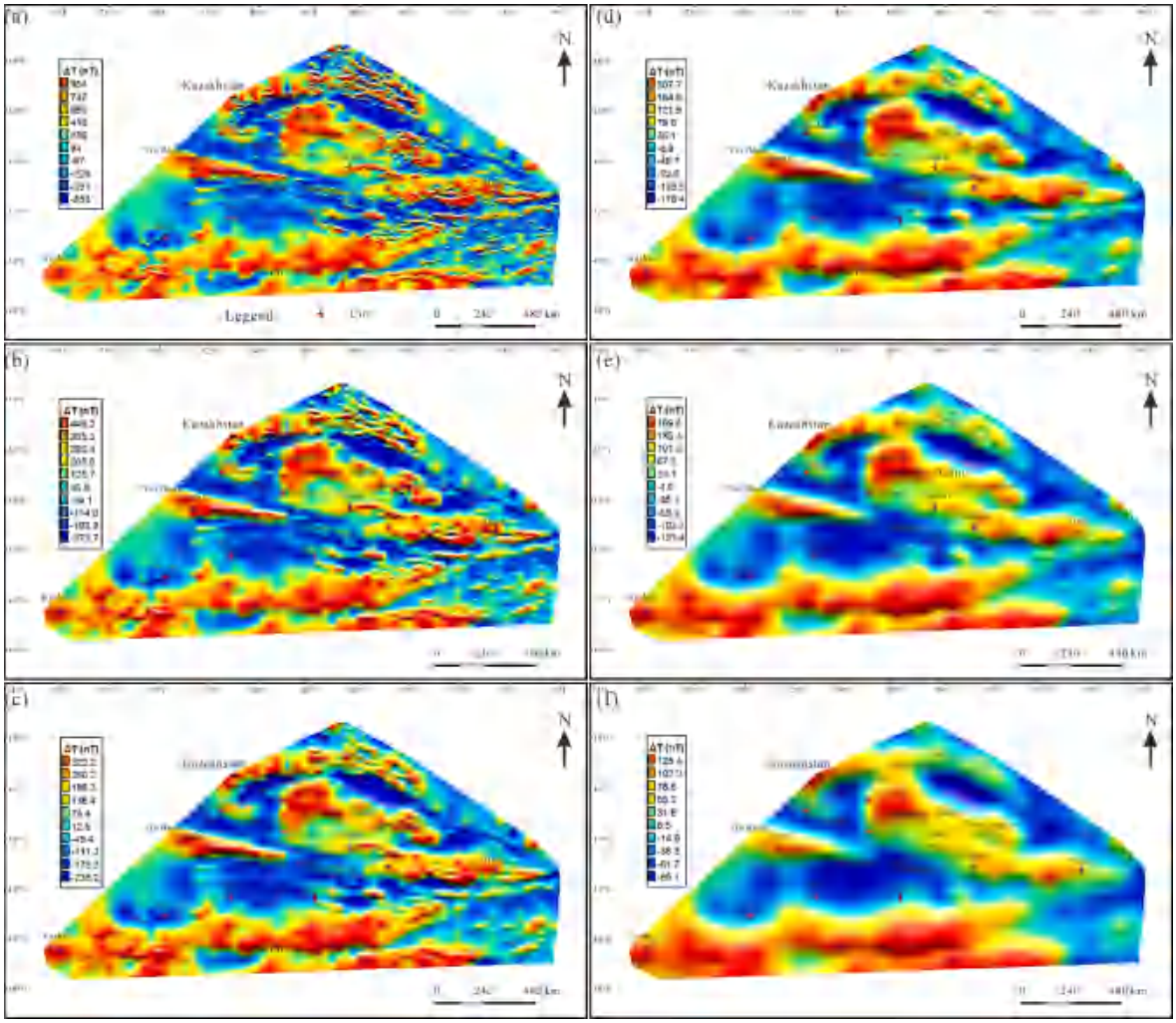

Fig. 3. Reduction to pole (RTP) maps. (a) Magnetic anomalies with reduction to pole; and processed RTP maps for heights of (b) 5,000 m, (c) 10,000 m, (d) 20,000 m, (e) 30,000 m, and (f) 50,000 m.

center of the body when the data acquisition station is far from the body. We conducted signal amplitude analysis using the magnetic data after RTP and upward continuation procedures at different heights (Fig. 7).

The inversion methodology applied to the magnetic data was based on the work of Bhattacharyya (1964, 1980), Sharma (1966), Rao and Babu (1991), and Li and Oldenburg (1996, 2000) (Figs. 8–9). A brief description of the inversion methodology has been presented by Zhu and Lu (2021). We now also briefly describe the procedure for 3-D inversion of the magnetic data. The study area was ~1,760 km × ~1,140 km in size, and the target depth range of the magnetic anomalies extended from the surface to a depth of 45 km (Figs. 8 and 9). The size of the 3-D grid was based on the requirements of the inversion accuracy, scale of the data, and calculation efficiency. We adopted a spline interpolation gridding method during the modeling process, with a total of 623,700 grid points in the mesh data. An initial magnetic susceptibility model was established based on the magnetic susceptibility range of the rocks and ores (Table 1). To reduce the noise interference from the magnetic anomalies in a small region of the shallow subsurface strata, we performed upward continuation to a height of 200 m based on the observed magnetic data, and these results were used for the inversion.

The Curie point depth is a theoretical surface with a temperature of approximately580°C,at which magnetic elements lose their magnetization (Bhattacharyya and Leu, 1975). It can provide an estimation of the paleotemperature of the study area. We estimated the spatial distribution of the Curie point depth (Fig. 10b) based on the aeromagnetic data presented in Fig. 2.

5. Results

5.1. Variations in magnetic anomalies

The magnetic anomalies in the Chinese Altai orogen are generally NW–SE-trending, and are locally superimposed by E–W-trending anomalies (Figs. 2 and 3). There are three main positive anomaly areas in the western part of the study area (from Xibodu to Fuyun), which exhibit strong SSE–NNW-trending magnetic anomalies. These anomalies are characterized by large amplitude values and sharp peaks, and they are distributed within a small area. In the northern Tacheng area and the southern margin of the Chinese Altai orogen, bead-like positive anomalies are distributed in an NW–SE orientation.

The Junggar Basin is generally characterized by strong anomalies (Figs. 2 and 3). Strong SSW–NNE-trending positive anomalies were identified in the northwestern side of the basin, NW–SE-trending, strip-shaped, strong positive anomalies were identified in the southwestern side, and an NE–SW-trending positive anomaly band was identified in the center of the basin. There is a large-scale negative magnetic anomaly zone in the south-central part of the basin, and there are strong positive and NW–SE-trending bead-like negative anomalies in the eastern part of the basin. As the upward continuation height increases (Fig. 3b–f), the high-frequency component of the magnetic anomaly gradually weakens,

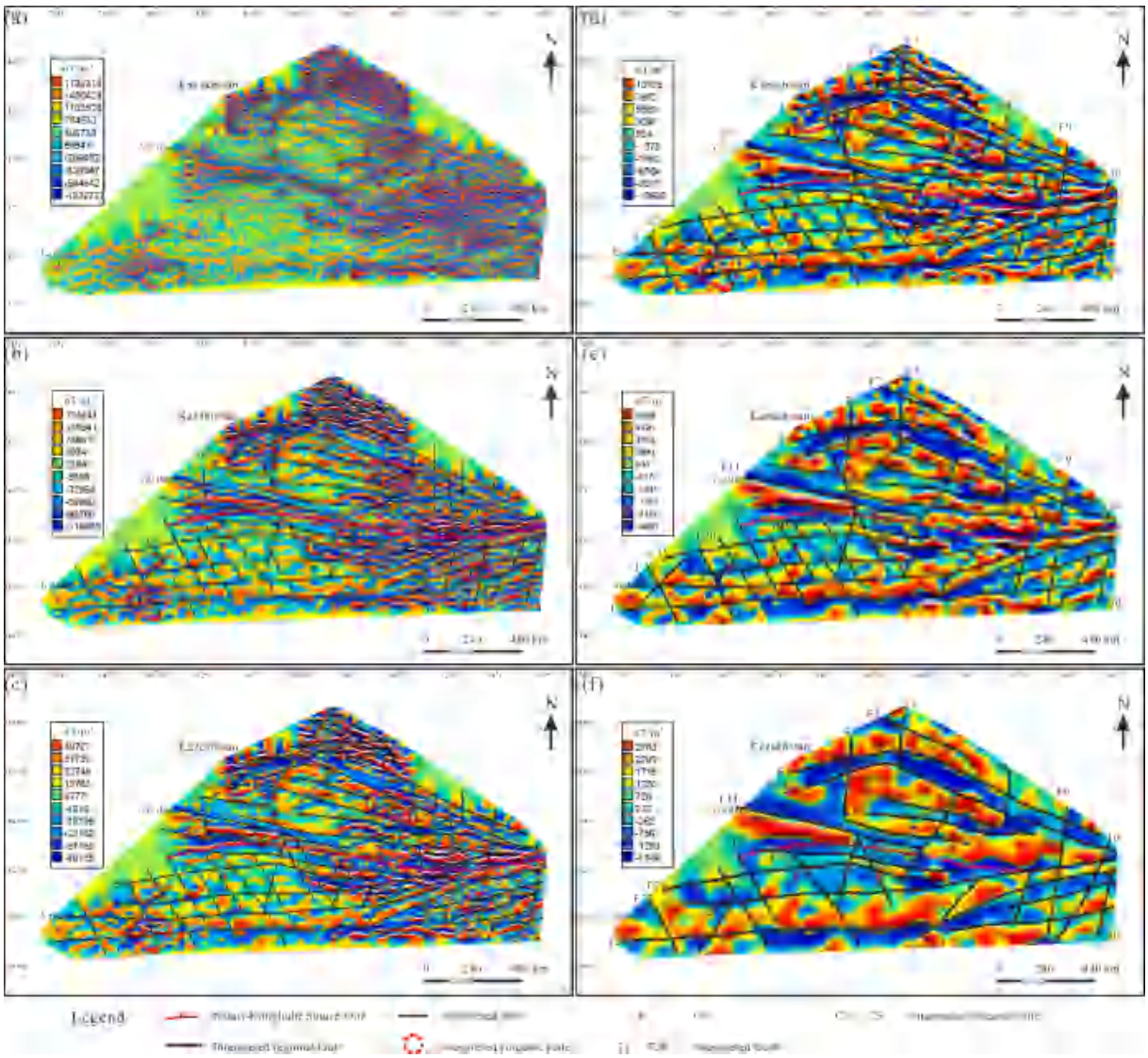

Fig. 4. (a) Second-order derivative in the vertical direction of the RTP map; and processed RTP maps for heights of (b) 5,000 m, (c) 10,000 m, (d) 20,000 m, (e) 30,000 m, and (f) 50,000 m.

and the low-frequency component gradually becomes more and more obvious and tends to become stable, revealing the magnetic anomaly properties of the basement.

The magnetic anomalies in the Galaultao Mountains, located to the north of Alashankou, are characterized by shallow gradients and low amplitude values, and they are distributed within a small area (Figs. 2 and 3). The anomalies are weak and exhibit elliptical and bead-like shapes, suggesting that they represent shallow intrusive bodies, possibly granodiorite intrusions, in the sedimentary strata.

The Alashankou area is dominated by strong magnetic anomalies that generally trend NNW–SSE. The magnetic anomaly variations in the northern part of this area are complex (Figs. 2 and 3). The positive and negative magnetic anomalies are oriented either NNW–SSE or E–W, revealing two major regional faulting patterns in this area.

The Tianshan Mountains and adjacent areas can be divided into three regions with distinct magnetic anomaly patterns (Figs. 2 and 3). The Tarim Basin to the south of the Tianshan Mountains is characterized by widely distributed strong positive magnetic anomalies, and large-scale positive magnetic anomalies were observed from the Junggar Basin to Hami, to the north of the mountains. Large-scale negative magnetic anomalies occur in the West Tianshan Mountains and the northern Tarim Basin.

The Tianshan Mountains can be divided along the line between Urumqi and Korla into a small negative magnetic anomaly area in the west and a complex area with both positive and negative anomalies in the east (Figs. 2 and 3). There are obvious differences in the characteristics of the magnetic anomalies in the East and West Tianshan Mountains. The latter are dominated by negative anomalies, and only the Yining Block, Awulale, and Nalati contain positive anomalies. The South Tianshan Mountains are characterized by negative magnetic anomalies. The magnetic anomalies in the central North Tianshan Mountains are similar to those in the Junggar Basin. The magnetic anomalies in the central Tianshan Mountains are oriented NNW–SSE and exhibit marked spatial variations, which is consistent with the trend of the regional structures in the North Tianshan Mountains. The magnetic anomalies in the Tianshan Mountains are generally weak. Positive NNW–SSE-trending magnetic anomalies were observed in the Karamay–Urumqi area.

Several main magnetic anomaly areas were identified in the West Tianshan Mountains. Of these, the Alatau-Irene Habirga area and South Tianshan Mountains are characterized by weak magnetic anomalies; the Dabancheng, Yining-Awulale Mountains, and Nalati area are dominated by strong magnetic anomalies; and the Nalati–Hongliuhe Suture (NHS) zone is characterized by strong anomalies (Figs. 2 and 3).

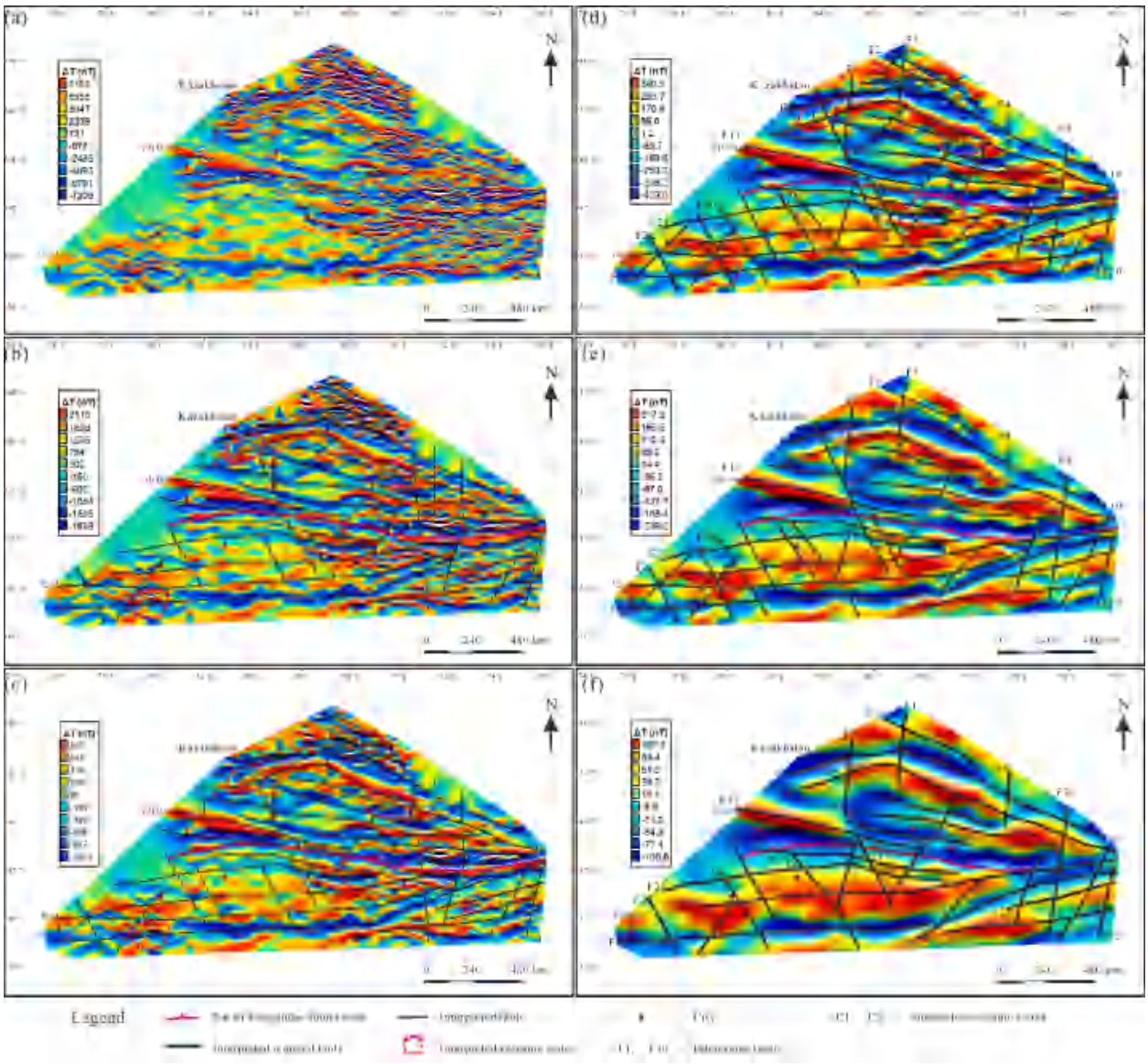

Fig. 5. (a) Boundary enhancement in the horizontal direction of the RTP map; and processed RTP maps for heights of (b) 5,000 m, (c) 10,000 m, (d) 20,000 m, (e) 30,000 m, and (f) 50,000 m.

The Yili Massif is characterized by both positive and negative magnetic anomalies with various spacings. A positive magnetic anomaly belt is located in the Qapqal–Gongliu area in the West Tianshan Mountains. This NNW–SSE-trending belt is located in the Yili Block, and in places, it is connected to the positive magnetic anomaly belt in the Kangur region of the East Tianshan Mountains.

In the Dabancheng area, extending from Kuitun in the west to Urumqi in the north, small and strong magnetic anomalies were observed, with strip-shaped strong magnetic anomalies superimposed locally (Figs. 2 and 3). These anomalies are mainly located where the Carboniferous and Permian volcanic clastic rock formations and mafic-ultramafic intrusive rocks occur.

Strong magnetic anomalies are distributed in a linear pattern along the NHS, which is located from Zhaosu County to the Dakendaban area (Figs. 2 and 3). This zone of magnetic anomalies represents the large volume of mafic-ultramafic rocks in the NHS zone. The northern Tarim Basin, located to the south of the suture zone and north of 40°N, is characterized by a large area of E–W-oriented negative magnetic anomalies. The southern Tarim Basin, located south of 40°N, is characterized by strong NE–SW-trending positive anomalies. The characteristics of the anomalies in this area are distinct from those in the northern Tarim Basin, indicating that the boundary fault zone separating the South and North Tarim blocks is located along ~40°N.

The East Tianshan Mountains are dominated by interjacent positive and negative magnetic anomalies, with slight variations in the size and characteristics of the anomalies in the eastern part, indicating a complex geology and structure (Figs. 2 and 3). In the Turpan–Hami Basin, small magnetic anomalies are distributed in an E–W-oriented band. Minor strong magnetic anomalies were also identified in the southwestern part of the basin.

5.2. *Structural features and distribution of magnetic bodies*

The faults in the Chinese Altai orogen are mainly oriented NW–SE and are superimposed by E–W-, NNE–SSW-, and N–S-trending structures (Figs. 4–7). The faults in the northern margin of the Junggar Basin mainly trend NW–SE and gradually transform to EW trending from north to south; whereas those in the western of the basin are mainly oriented NE–SW and N–S. In West Junggar, the faults are mostly NE–SW-trending, accompanied by NW–SE-, N–S-, and E–W-trending secondary faults.

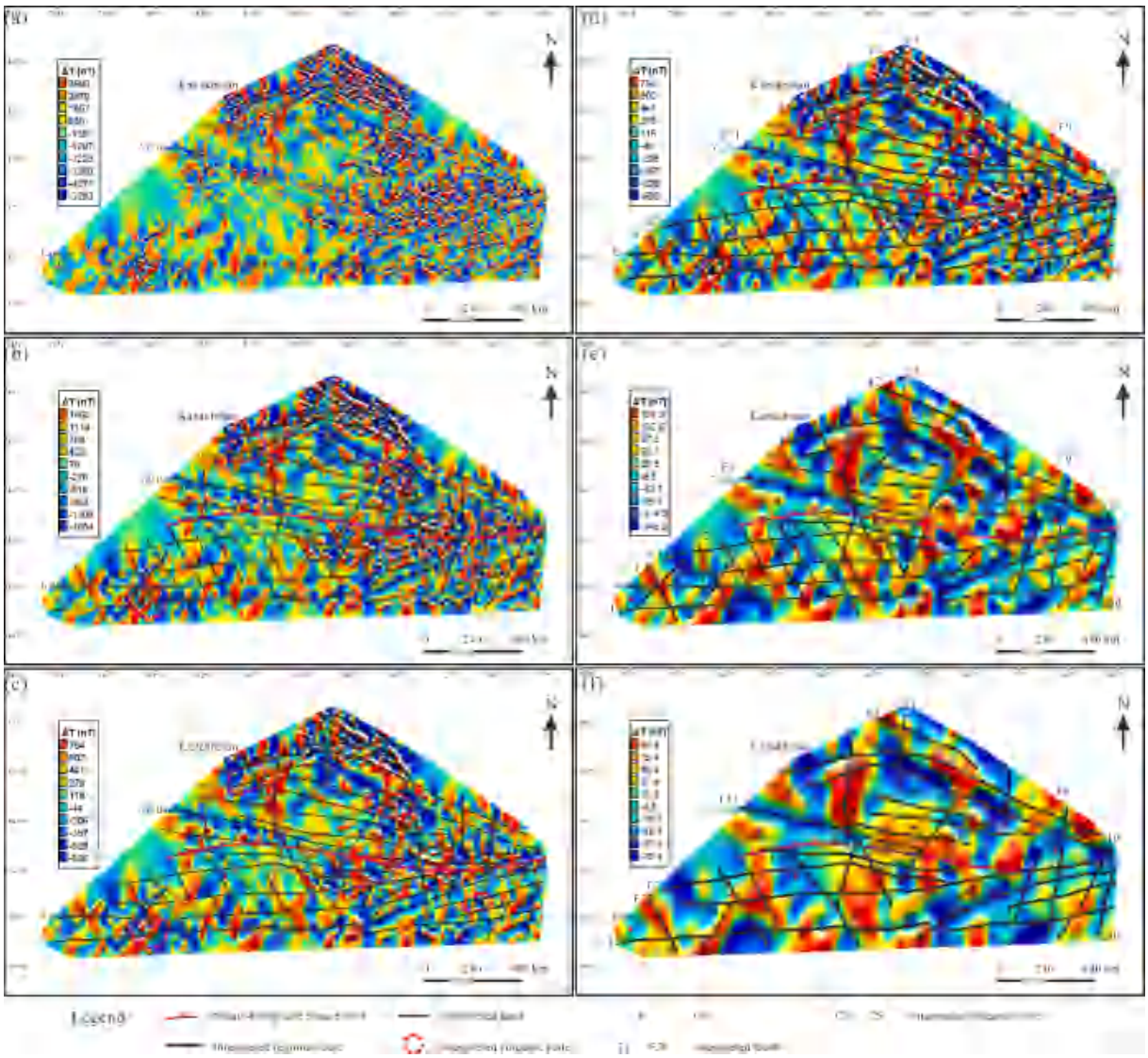

Fig. 6. (a) Boundary enhancement in the vertical direction of the RTP map; and processed RTP maps for heights of (b) 5,000 m, (c) 10,000 m, (d) 20,000 m, (e) 30,000 m, and (f) 50,000 m.

The faults in the Tianshan Mountains are well developed (Figs. 4–7). The main faults are oriented NW–SE or E–W and are locally superimposed by NNE–SSW- and NNW–SSE-trending conjugate faults. The faults in the Tianshan Mountains can be divided into three groups according to their strikes. The first group is a combination of E–W- and nearly E–W-trending faults, which extend for tens or hundreds of kilometers. These faults were generated as a result of N–S crustal compression, which also formed compressive or torsional structural planes. The second group consists of NE–SW-trending faults and secondary faults associated with thrust-nappe structures. The third group is characterized by NW–SE-trending faults that occur where the volcanic rocks are well developed.

In the NHS, the faults are mainly NNE–SSW-trending in the west and gradually transform to nearly E–W-, NNW–SSE-, and NNE–SSW-trending toward the east (Figs. 4–7). In the northern Tarim Basin, the faults are predominantly nearly E–W trending and are superimposed by NW–SE- and NE–SW-trending secondary faults.

In addition to those in the NHS, several deep regional faults were revealed by the patterns in the magnetic anomaly maps (Figs. 4–7). These regional faults are faults F5 and F6 between the Altay and Junggar basins, fault F3 in Southwest Junggar, and faults F26 and F27 in the northern Tarim Basin. These faults cut through the Moho and mark the collision zones between the tectonic plates and/or microcontinents.

The final 3-D magnetic inversion revealed the distribution of the magnetic bodies in the study area encompassing the Chinese Altai, Junggar Basin, Tianshan Mountains, and Tarim Basin (Figs. 8–9). The pattern of the high magnetic susceptibility anomalies is mostly consistent with the known geology. In general, the distribution of the strongly magnetic materials (Fig. 8b–f) is in good agreement with the spatial distribution of the igneous rocks (Fig. 1). According to the slices at different depths in the 3-D inversion model, the high magnetic susceptibility values in West Junggar, eastern Chinese Altai orogen, and central East Tianshan Mountains gradually increase with increasing depth, the high magnetic susceptibility value in the northern Tarim Basin become more obvious with depth, and the magnetic susceptibility of the NHS becomes more prominent from east to west. The structural features indicated by the magnetic susceptibility patterns at different depths (i.e., 9, 18, 27, 36, and 42 km; Fig. 8b–f) and at different distances from west to east (e.g., 300, 620, 800, 900, 1100, 1400, and 1600 km; Fig. 9b–h) are consistent with the interpreted faults and volcanic units shown in Figs. 4–7. Most of the interpreted faults are consistent with the locations of the steep vertical gradients in the magnetic susceptibility in the sections (Fig. 9b–h).

The volcanic structures in the study area are mostly remnants of

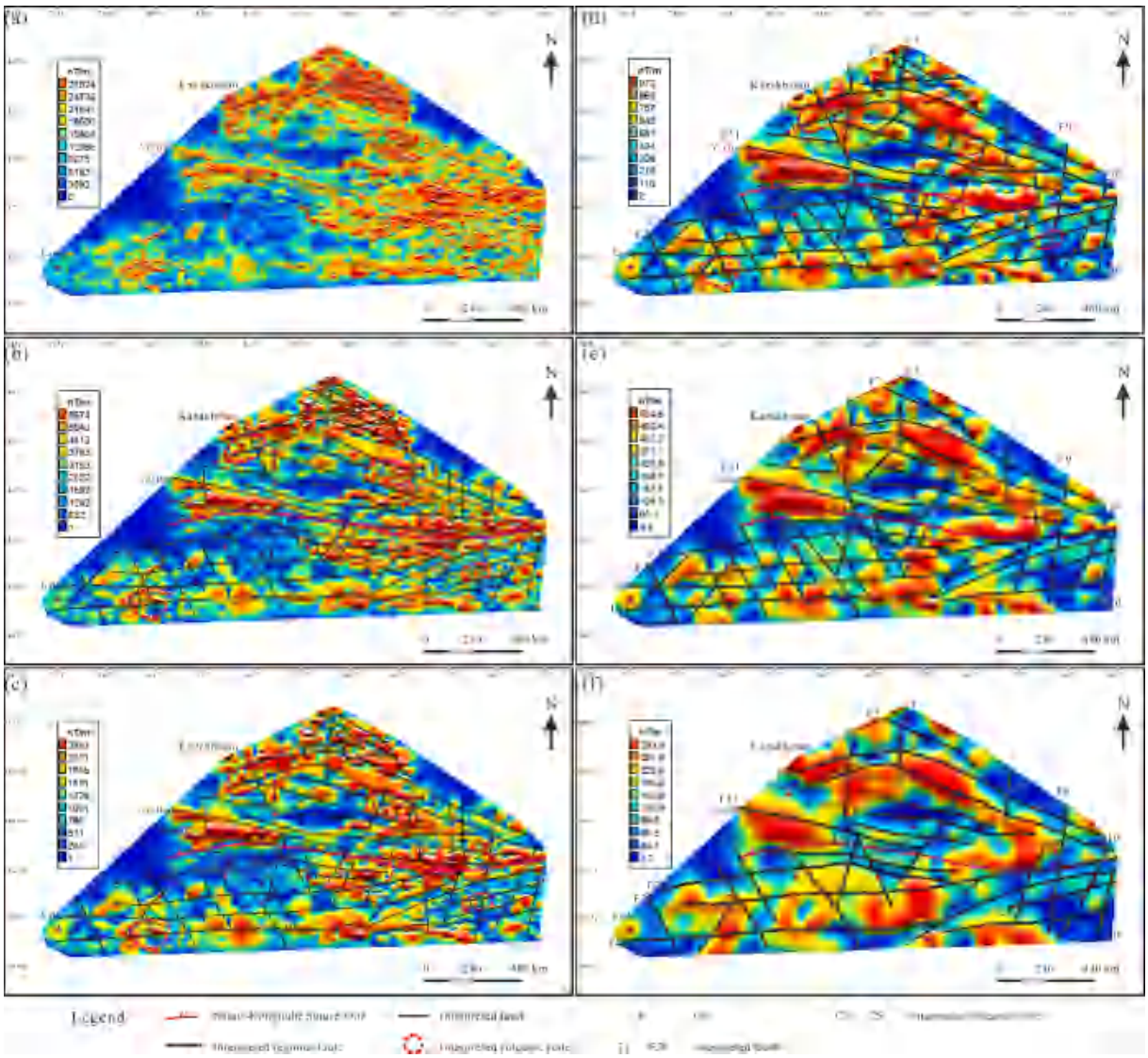

Fig. 7. (a) Signal amplitude of the RTP map; and processed RTP maps for heights of (b) 5,000 m, (c) 10,000 m, (d) 20,000 m, (e) 30,000 m, and (f) 50,000 m.

ancient volcanism, which have been modified by subsequent geological processes. The rocks in these structures include plutonic, hypabyssal, volcanic, and pyroclastic rocks (Zhu and Lu, 2016, 2021; Zhu et al., 2019, 2022). On the magnetic anomaly map (Figs. 2 and 3), the volcanic structures are mostly evident as large, alternating positive and negative annular magnetic anomaly belts, single annular and equiaxial anomalies, and clusters of anomalies distributed in chains along faults. Five regional volcanic structures (C1–C5) were identified (Figs. 4–7). The distribution of the magnetic anomalies and the patterns of the magnetic susceptibility body model obtained through inversion closely correspond to the distribution of the volcanic structures in West Junggar, Junggar Basin, Tianshan Mountains, and Tarim Basin. Most of the volcanic structures (C1–C4) are composed of mantle material and material formed by deep-source magmatic melting, which upwelled along the deep faults that cut through the crust during plate subduction.

The distributions of the fault structures shown in Figs. 4–7, 8, and 9 are based on the interpreted faults and regional volcanic structures (C1–C5) (Fig. 10a). We inferred the presence of one suture zone (NHS) and 30 regional faults (F1–F30), the strikes and magnetic properties of which are listed in Table 2.

6. Discussion

6.1. Nature of the basement of the Junggar Basin

Several viewpoints have been proposed regarding the nature of the basement of the Junggar Basin. Several previous studies have suggested the existence of Precambrian crystalline basement in the Junggar Basin (Ren, 1984; Wang, 1986; Wu, 1986), whereas others have argued that the basin's crust is composed of Paleozoic oceanic crustal material, with no rigid ancient basement (Jiang, 1984; Li, 1985, 1986; Coleman, 1989; Feng et al., 1989), or that it is mainly composed of small Paleozoic oceanic basins, initial-oceanic basins, and oceanic-basin sedimentary folds, as well as possible remnants of small ancient continental blocks (Xiao et al., 1994).

The magnetic anomaly pattern of the study area (Figs. 3–7) shows that the Junggar Basin is characterized by strong anomalies and that the characteristics and pattern of the magnetic anomalies vary little with increasing depth (Fig. 8). The Junggar Basin is also characterized by high gravity anomalies (Jiang, 1985; Zheng et al., 2021).

The Curie point depths are deep (~30–42 km) in the Junggar Basin, indicating that this region is characterized by depression in general (Fig. 10b). The Curie point isotherm surface is high in West Junggar, East Junggar, and the northern margin of the basin, indicating that these

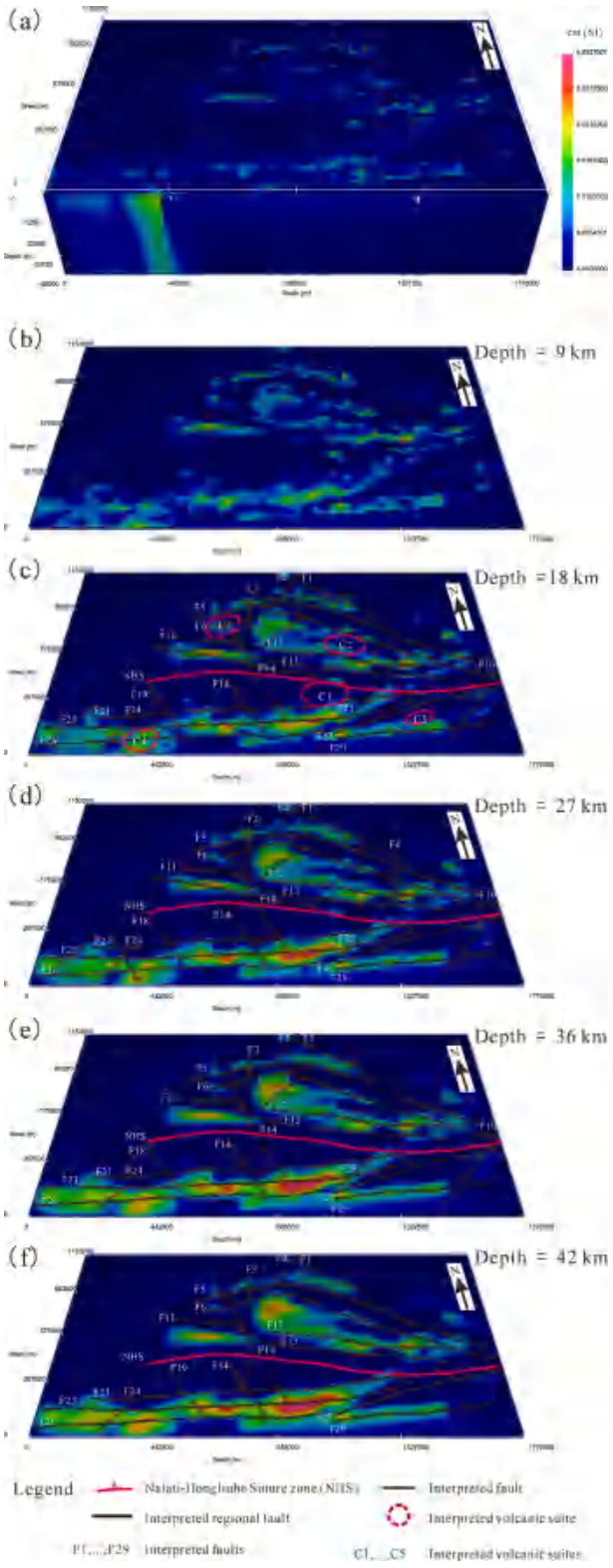

Fig. 8. (a) Spatial distribution of magnetic susceptibility obtained from 3-D magnetic inversion; and magnetic susceptibility sections at depths of (b) 9,000 m, (c) 18,000 m, (d) 27,000 m, (e) 36,000 m, and (f) 50,000 m. The interpreted faults are those shown in Fig. 4.

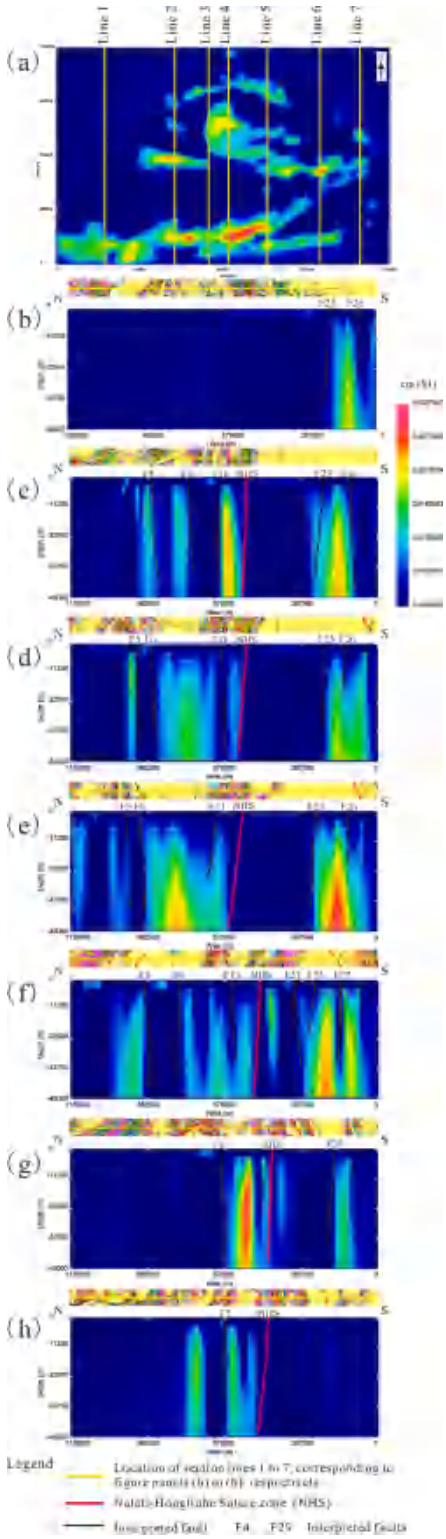

Fig. 9. Sections of 3-D inversion results. (a) Schematic diagram showing the locations of the seven sections; and (b–h) the distribution of the magnetic susceptibility along lines 1–7, respectively. The seven parts of the geological map along lines 1–7 are shown in Fig. 1.

regions are uplift areas (Fig. 10b). It is speculated that the geothermal gradient and heat flow values in the Junggar Basin are lower than those in the surrounding areas.

According to a map of the crustal thickness in the study area (Fig. 10c), the crustal underlying the Junggar Basin is ~40 km thick (Laske et al., 2021). The Moho (i.e., crustal thickness) under the Junggar Basin is nearly flat, while the Moho under the northern, southern and eastern margins of the basin rapidly descends from the basin outwards and becomes deeper (Fig. 10c). Broadband seismic observations provide

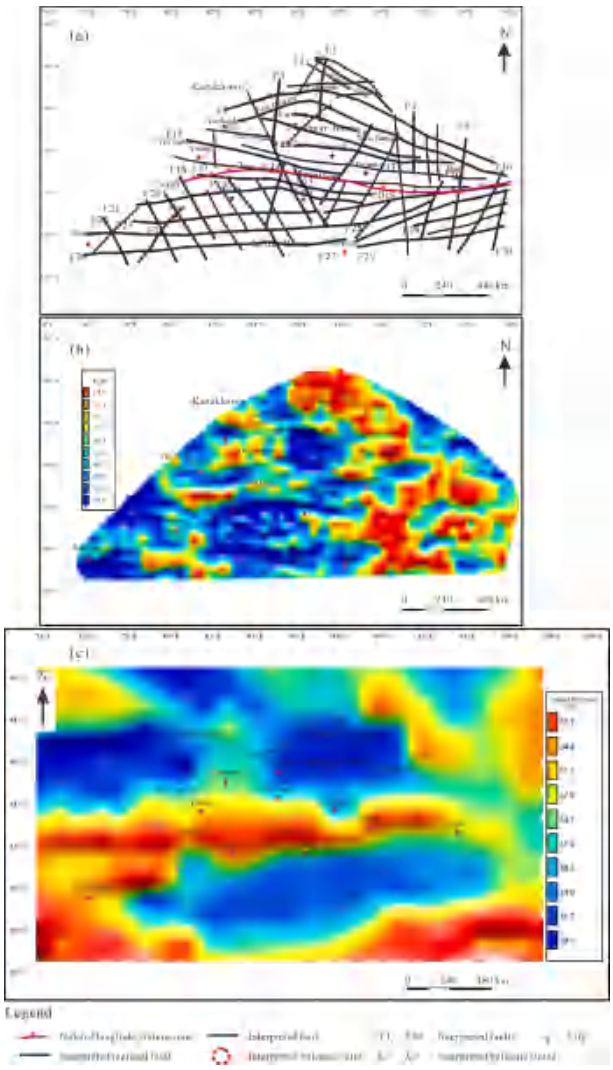

Fig. 10. (a) Outline map showing the faults and volcanic suites interpreted from the aeromagnetic measurements in the Chinese Altai, Junggar Basin, Tianshan Mountains, and Tarim Basin regions; (b) map of the Curie point depth calculated based on the aeromagnetic data shown in Fig. 2; and (c) map of the crustal thickness (Laske et al., 2021). NHS is the interpreted Nalati–Hongliuhe Suture zone, the regional faults are labeled F1–F30, and the volcanic suites are labeled C1–C5.

support for NW–SE-directed paleo-subduction, during which an oceanic slab became trapped beneath SW Junggar (Zhang et al., 2011; Wu et al., 2018; Zheng et al., 2021). All of the results described above suggest that the basement of the Junggar Basin is composed of oceanic crustal material (Yang et al., 2022) or continental-like material (such as back-arc basin or continental accretionary margin lithologies with volcanic intrusions) (Fig. 10).

6.2. Upwelling of mantle material in West Junggar

The upwelling of mantle material in the West Junggar orogenic belt is a mirror image of the foreland depression in the northwestern Junggar Basin. The Junggar Basin was located in an extensional zone caused by upwelling mantle, whereas the orogenic belt of West Junggar was dominated by the convergence of the mantle flow triggered by the downward motion of the subducting oceanic crust (Qian et al., 2011; Xu et al., 2020; Zheng et al., 2021). The Early Paleozoic oceanic crust material of the Junggar Plate may still be present in the middle and lower crust of the NW Junggar Basin, whereas mafic–ultramafic mantle-derived material is inferred to be widely distributed in the middle and lower crust in the Karamay region, which is consistent with the characteristics of the magnetic anomalies there (Figs. 3–7) (Qiu and Li, 2002; Xu et al., 2020).

Table 2
Regional faults and their features based on magnetic data for the Chinese Altai orogen, Junggar Basin, Tianshan Mountains, and Tarim Basin.

Fault name	Fault strike	Magnetic field characteristics
NHS	ENE-WSW	Gradient variation belt, discontinuity
F1	N-S	Gradient variation belt, dislocation
F2	NW-SE	Gradient variation belt, dislocation
F3	N-S	Gradient variation belt, discontinuity
F4	N-S	Gradient variation belt, dislocation
F5	NE-SW	Gradient variation belt, discontinuity
F6	NE-SW	Gradient variation belt, discontinuity
F7	NW-SE	Gradient variation belt, discontinuity
F8	NNE-SSW	Gradient variation belt, dislocation
F9	NNE-SSW	Bead-like anomaly belt, dislocation
F10	NE-SW	Bead-like anomaly belt, dislocation
F11	NW-SE	Gradient variation belt, discontinuity
F12	NW-SE	Gradient variation belt, discontinuity
F13	NW-SE	Gradient variation belt, discontinuity
F14	NNE-SSW	Gradient variation belt, dislocation
F15	NNW-SSE	Bead-like anomaly belt, dislocation
F16	NNE-SSW	Bead-like anomaly belt, dislocation
F17	NW-SE	Gradient variation belt, discontinuity
F18	NNW-SSE	Bead-like anomaly belt, dislocation
F19	NNW-SSE	Bead-like anomaly belt, dislocation
F20	NNW-SSE	Bead-like anomaly belt, dislocation
F21	E-W	Gradient variation belt, discontinuity
F22	NNW-SSE	Gradient variation belt, dislocation
F23	E-W	Gradient variation belt, discontinuity
F24	NE-SW	Gradient variation belt, dislocation
F25	NE-SW	Gradient variation belt, dislocation
F26	E-W	Gradient variation belt, discontinuity
F27	NNE-SSW	Gradient variation belt, discontinuity
F28	NNE-SSW	Bead-like anomaly belt, discontinuity
F29	E-W	Gradient variation belt, discontinuity
F30	NNE-SSW	Bead-like anomaly belt, dislocation

During the Paleozoic, the northwestern Junggar Basin was dominated by an extensional environment, and its lower mantle material was characterized by upwelling due to the thermal and equilibrium effects of the crustal and mantle materials, which is consistent with the pattern of the magnetic anomalies in this area (Figs. 3–7). This mantle upwelling led to subsidence of the Junggar Basin, and thick sedimentary deposits were formed in response (Qiu, 1989). During the Devonian–Late Carboniferous, West Junggar converged toward the Junggar Basin as a result of movement of the Kazakhstan Plate, and the Junggar Basin was subducted under the West Junggar orogenic belt, resulting in the formation of a foreland basin during the Late Carboniferous (Qiu and Li, 2002; Zhang et al., 2012; Xu et al., 2020).

6.3. Stages of deformation in West Junggar

West Junggar underwent several stages of deformation during the Late Carboniferous–Cretaceous (Han et al., 2006; Xu et al., 2006; Zhang et al., 2011, 2012; Zhao et al., 2011). During the Late Carboniferous, with the final closure of the residual ocean basin in West Junggar between the Kazakhstan and Junggar plates, this region was affected by multiple episodes of collisional orogenesis, forming a series of nearly N–S-trending fold-thrust structures, NE–SW-trending fold–fault assemblages, and ophiolitic mélanges (Figs. 3–7) (Han et al., 2006; Xu et al., 2006; Zhang et al., 2011, 2012).

During the Late Permian–Late Triassic, a nearly E–W-trending regional subvertical cleavage formed in the rocks of Mount Zaire, indicating nearly N–S-oriented compression (Figs. 3–7) (Zhang et al., 2011). During this period, the tectonic deformation in NW Junggar originated from the N–S-directed compression across this region and included the formation of a foreland and depression basin (Figs. 3–7) (Meng et al.,

2009).

Continental basalts derived from a depleted mantle source were emplaced in the southwestern foothills of the Karamay area and unconformably overlie the Early Jurassic Badaowan Formation (Figs. 3–7). The age of these basalts is 192.7 ± 1.3 Ma, which indicates that NW Junggar was in an extensional environment during the Early Jurassic (Yang et al., 2012; Zhang et al., 2021). Previous studies have identified Late Triassic rhyolites and basalts (220–202 Ma) and Middle Jurassic igneous rocks (170.6 Ma) in the Karamay-Baikouquan area, indicating that NW Junggar was in an extensional tectonic regime during the Late Triassic–Early Middle Jurassic (Su et al., 2006; Xu et al., 2006; Geng et al., 2009).

The broad and gentle fold structures of NW Junggar that formed during the Late Triassic and the parallel (or angular) unconformity between the Upper Triassic and Lower Jurassic rocks indicate that a short-duration tectonic inversion occurred at the Late Triassic–Early Jurassic boundary (Figs. 3–7). The northwestern margin of the Junggar Basin underwent uplift caused by tectonic compression during the Middle Jurassic–Early Cretaceous and was formed as a compressional depression basin.

7. Conclusions

We used magnetic data combined with regional geological information to infer the distribution of the magnetic anomalies in the region across the Chinese Altai orogen, Junggar Basin, Tianshan orogen, and Tarim Basin and to reveal the presence and distribution of the deep fault structures and igneous bodies with high magnetic susceptibilities in this area.

(1) The magnetic anomalies in the Chinese Altai orogen are generally NW–SE trending. The anomalies in the Tianshan Mountains are mainly oriented E–W and nearly E–W, with NNE–SSW- and NNW–SSE-trending anomalies superposed locally. The anomalies in the northern Tarim Basin are generally nearly E–W trending. The strong positive anomalies in the Junggar Basin trend NNE–SSW in the northwest, NW–SE in the southwest, and NE–SW in the center, revealing the presence of many deep faults (or linear tectonics).
(2) We suggest that the basement of the Junggar Basin is composed of oceanic crustal material or continental-like material (such as back–arc basin or continental accretionary margin lithologies with volcanic intrusions) based on the magnetic, gravity, and crustal-thickness data. The results of this study constrain the occurrence of mantle material upwelling in West Junggar, as well as the stages of deformation in the study area during the Late Carboniferous–Cretaceous.

Our findings based on magnetic data are significant for understanding the geology, basement crustal structures, and geodynamic evolution of the NW CAOB.

CRediT authorship contribution statement

Xiaosan Zhu: Conceptualization, Methodology, Data curation, Software, Investigation, Writing – original draft, Writing – review & editing. **Tao Wang:** Resources, Writing – review & editing. **He Huang:** Resources, Writing – review & editing. **Hongwei Zheng:** Data curation, Visualization.

Declaration of Competing Interest

The authors declare that they have no known competing financial interests or personal relationships that could have appeared to influence the work reported in this paper.

Acknowledgments

This work was jointly funded by the Ministry of Science and Technology of the People's Republic of China (No. 2019YFA0708601-02), the National Natural Science Foundation of China (Nos. 41404070 and 42174172), and the China Geological Survey (Nos. DD20221647 and DD20221649).

References

Baranov, V., 1957. A new method for interpretation of aeromagnetic maps: pseudo-gravimetric anomalies. Geophysics 22, 359–383.
Baranov, V., Naudy, H., 1964. Numerical calculation of the formula of reduction to the magnetic pole. Geophysics 29, 67–79.
Bhattacharyya, B.K., 1964. Magnetic anomalies due to prism–shaped bodies with arbitrary magnetization. Geophysics 29, 517–531.
Bhattacharyya, B.K., Leu, L.K., 1975. Analysis of magnetic anomalies over Yellowstone National Park: Mapping of Curie point isothermal surface for geothermal reconnaissance. J. Geophys. Res. 80, 4461–4465.
Bhattacharyya, B.K., 1980. A generalized multibody model for inversion of magnetic anomalies. Geophysics 45, 255–270.
Biedermann, A.R., McEnroe, S.A., 2017. Effects of magnetic anisotropy on total magnetic field anomalies. Journal of Geophysical Research – Solid Earth 122 (11), 8628–8644.
Buchko, I.V., Sorokin, A.A., Izokh, A.E., Larin, A.M., Kotov, A.B., Sal'nikova, B., Velikoslavinskii, S.D., Sorokin, S.Z., Yakovleva, A.P., Plotkina, Y.V., 2008. Petrology of the Early Mesozoic ultramafic-mafic Lu China massif (southeastern periphery of the Siberian craton). Russian Geology and Geophysics, 49, 570-581.
Chen, Y., Xiao, W., Windley, B.F., Zhang, J., Zhou, K., Sang, M., 2017. Structures and detrital zircon ages of the Devonian-Permian Tarbagatay accretionary complex in west Junggar, China: imbricated ocean plate stratigraphy and implications for amalgamation of the CAOB. Int. Geol. Rev. 59 (9), 1097–1115. https://doi.org/10.1080/00206814.2016.1185652.
Clark, D.A., 1997. Magnetic petrophysics and magnetic petrology: aids to geological interpretation of magnetic surveys. J. Australian Geol. Geophys. 17, 83–103.
Clark, D.A., 2014. Methods for determining remanent and total magnetizations of magnetic sources – a review. Explor. Geophys. 45, 271–304.
Coleman, R.G., 1989. Continental growth of Northwest China. Tectonics 8 (3), 621–635. https://doi.org/10.1029/TC008i003p00621.
Feng, Y., Coleman, R.G., Tilton, G., Xiao, X., 1989. Tectonic evolution of the west Junggar region, Xinjiang, China. Tectonics 8 (4), 729–752. https://doi.org/10.1029/TC008i004p00729.
Gao, J., Klemd, R., Zhu, M., Wang, X., Li, J., Wan, B., Xiao, W., Zeng, Q., Shen, P., Sun, J., Qin, K., Campos, E., 2018. Large-scale porphyry-type mineralization in the Central Asian metallogenic domain: A review. J. Asian Earth Sci. 165, 7–36.
Gao, R., Xiao, X., Kao, H., Li, Q., Liu, X., Jiang, M., Shi, D., 2002. Summary of deep seismic probing of the lithospheric structure across the West Kunlun–Tarim–Tianshan. Geological Bulletin of China 21 (1), 11–20 in Chinese with English abstract.
Geng, H., Sun, M., Yuan, C., Xiao, W., Xian, W., Zhao, G., Zhang, L., Wong, K., 2009. Geochemical, Sr-Nd and zircon U-Pb-Hf isotopic studies of Late Carboniferous magmatism in the west Junggar, Xinjiang: Implications for ridge subduction? Chem. Geol. 266 (3–4), 364–389. https://doi.org/10.1016/j.chemgeo.2009.07.001.
Guo, J., Shu, L., Charvet, J., Laurent-Charvet, S., Sun, S., 2002. Geochemical features of the two early Paleozoic ophiolitic zones and the volcanic rocks in the Central-Southern Tianshan region, Xinjiang. Chin. J. Geochem. 21, 308–321.
Guy, A., Schulmann, K., Soejono, I., Xiao, W., 2020. Revision of the Chinese Altai-East Junggar terrane accretion model based on geophysical and geological constraints. Tectonics, 39, e2019TC006026. https://doi.org/ 10.1029/2019TC006026.
Han, B., Ji, J., Song, B., Chen, L., Zhang, L., 2006. Late Paleozoic vertical growth of continental crust around the Junggar Basin, Xinjiang, China (Part I): Timing of post-collisional plutonism. Acta Petrologica Sinica 22 (5), 1077–1086 in Chinese with English abstract.
Han, Y., Zhao, G., 2018. Final amalgamation of the Tianshan and Junggar orogenic collage in southwestern Central Asian Orogenic Belt: Constraints on the closure of the Paleo-Asian Ocean. Earth Sci. Rev. 186, 129–152.
Henderson, R., 1970. On the validity of the use of the upward continuation integral for total magnetic intensity data. Geophysics 35 (5), 916–919.
Jacobsen, B., 1987. A case for upward continuation as a standard separation filter for potential–field maps. Geophysics 52, 1138–1148.
Jahn, B.M., Wu, F., Chen, B., 2000. Granitoids of the Central Asian Orogenic Belt and continental growth in the Phanerozoic. Trans R Soc Edinb Earth Sci 91, 181–193.
Ji, J., Li, H., Zhang, L., 1999. Sm–Nd and Rb–Sr isotopic ages of magnetite–chlorite formation gold deposit in the volcanic rock area of Late Paleozoic Era, East Tianshan. Chin. Sci. Bull. 44, 1801–1804.
Jiang, Y., 1984. A Preliminary approach to the basement of Junggar district. Xingjiang Geology 2 (1), 11–16 in Chinese with English abstract.
Jiang, Y., 1985. Study of deep structure by data of regional geophysical survey in Tianshan and Junggar region, Xinjiang. Xingjiang Geology 4, 51–57 in Chinese with English abstract.
Jiang, Y., Schulmann, K., Sun, M., Štípská, P., Guy, A., Janoušek, V., Lexa, O., Yuan, C., 2016. Anatexis of accretionary wedge, Pacific-type magmatism, and formation of vertically stratified continental crust in the Altai Orogenic Belt. Tectonics, 35, 3095-3118. https://doi.org/ 10.1002/2016TC004271.

Kadasi, A.N., 2015. Interpretation of aeromagnetic data in terms of surface and subsurface geologic structures, southwestern Yemen. Arab J Geosci 8, 1163–1179.
Laske, G., Ma, Z., Masters, G., Pasyanos, M., 2021. A new global crustal model at 1x1 degree (Crust 1.0). https://igppweb.ucsd.edu/~gabi/crust1.html.
Li, C., 1985. Discussion on the division of continental paleoplates. China Geology 1, 13–16 in Chinese.
Li, C., 1986. On Terrane. Geological Review 32 (6), 578–582 in Chinese with English abstract.
Li, C., Wang, S., Wang, L., 2019. Tectonostratigraphic history of the southern Tian Shan, western China, from seismic reflection profile. J. Asian Earth Sci. 172, 101–114.
Li, D., He, D., Tang, Y., 2016. Reconstructing multiple arc-basin systems in the Altai–Junggar area (NW China): Implications for the architecture and evolution of the western Central Asian Orogenic Belt. J. Asian Earth Sci. 121, 84–107. https://doi.org/10.1016/j.jseaes.2016.02.010.
Li, J., He, G., Xu, X., Li, H., Sun, G., Yang, T., Gao, L., Zhu, Z., 2006. Crustal tectonic framework of northern Xinjiang and adjacent regions and its formation. Acta Geol. Sin. 80, 149–168 in Chinese with English abstract.
Li, L., Xiao, W., Windley, B.F., Mao, Q., Jia, X., Yang, H., Tan, Z., Sang, M., Gan, J., Abuduxun, N., 2021. Contrasting Early Palaeozoic provenance of the Yemaquan and Harlik arcs in the SW Altaids (NW China): identification of cryptic sutures in accretionary orogens. Int. Geol. Rev. 63 (17), 2192–2214.
Li, Y., Oldenburg, D.W., 1996. 3-D inversion of magnetic data. Geophysics 61, 394–408.
Li, Y., Oldenburg, D.W., 2000. Joint inversion of surface and three-component borehole magnetic data. Geophysics 65, 540–552.
Li, Z., Huang, B., Xiao, W., Yang, L., Qiao, Q., 2015. Paleomagnetic study of Late Paleozoic rocks in the Tacheng Basin of West Junggar (NW China): Implications for the tectonic evolution of the Western Altaids. Gondwana Res. 27, 862–877.
Liu, X., Xiao, W., Xu, J., Castillo, P.R., Shi, Y., 2017. Geochemical signature and rock associations of ocean ridge–subduction: Evidence from the Karamaili Paleo-Asian ophiolite in east Junggar, NW China. Gondwana Res. 48, 34–49.
Long, X., Yuan, C., Sun, M., Xiao, W., Zhao, G., Wang, Y., Cai, K., Xia, X., Xie, L., 2010. Detrital zircon U-Pb ages and Hf isotopes of the early Paleozoic flysch sequence in the Chinese Altai, NW China: new constrains on depositional age, provenance and tectonic evolution. Tectonophysics 480, 213–231.
Meng, J., Guo, Z., Fang, S., 2009. A new insight into the thrust structures at the northwestern margin of Junggar Basin. Earth Sci. Front. 16 (3), 171–180 in Chinese with English abstract.
Miller, H., Singh, V., 1994. Potential field titl–A new concept for location of potential field soutce. J. Appl. Geophys. 32 (2), 213–217.
Molnar, P., Tapponnier, P., 1975. Cenozoic tectonics of Asia: effects of continental collision. Science 189, 419–426.
Nabighian, M.N., 1972. The analytic signal of two-dimensional magnetic bodies with polygonal cross-section: its properties and use for automated anomaly interpretation. Geophysics 37 (3), 507.
Qian, H., Jiang, M., Xiao, W., Zhao, D., Wang, Y., Zhang, L., Zhao, L., 2011. Seismic tomography of Tianshan–Junggar region and its lithospheric structure. Acta Seismological Sincia 33 (3), 327–341 in Chinese with English abstract.
Qiu, D., 1989. Analysis of the Carboniferous sedimentary basins in northwest China. Lithofacies Palaeogeography 42, 1–12 in Chinese with English abstract.
Qiu, D., Li, X., 2002. The basin–range coupling and hydrocarbon generation: An example from northwestern Junggar Basin. Sedimentary Geology and Tethyan Geology 22 (3), 6–12 in Chinese with English abstract.
Ranganai, R.T., Whaler, K.A., Ebinger, C.J., 2016. Aeromagnetic interpretation in the south central Zimbabwe Craton: (reappraisal of) crustal structure and tectonic implications. Int. J. Earth Sci. (Geol Rundsch) 105, 2175–2201. https://doi.org/10.1007/s00531-015-1279-7.
Rao, D., Babu, N.R., 1991. A rapid methods for threedimensional modeling of magnetic anomalies. Geophysics 56, 1729–1737.
Ren, J., 1984. The Indosinian orogeny and its significance in the tectonic evolution of China. Bull. Chinese Acad. Geol. Sci. 9, 31–44 in Chinese with English abstract.
Ren, J., 2015. International geological map of Asia (1:5,000,000). Geological Publishing House, Beijing.
Şengör, A.M.C., Natal'in, B.A., Burtman, V.S., 1993. Evolution of the Altaid tectonic collage and Palaeozoic crustal growth in Eurasia. Nature 364, 299–307.
Şengör, A.M.C., Natal'in, B.A., 1996. Turkic-type orogeny and its role in the making of the continental crust. Annu Rev Earth Planet Sci 24, 263–337.
Sharma, P.V., 1966. Rapid computation of magnetic anomalies and demagnetization effects caused by bodies of arbitrary shape. Pure Appl Geophys 64, 89–109.
Sorokin, A.A., Kotov, A.B., Sal'nikova, E.B., Kudryashov, N.M., Anisimova, I.V., Yakovleva, S.Z., Fedoseenko, A.M., 2010. Granitoids of the Tyrma-Bureya complex in the northern Bureya-Jiamusi superterrane of the Central Asian Fold Belt: age and geodynamic setting. Russian Geology and Geophysics, 51, 563-571.
Su, Y.P., Tang, H.F., Hou, G.S., Liu, C.Q., 2006. Geochemistry of aluminous A-type granites along Darabut tectonic belt in west Junggar, Xinjiang. Geochemistry 35, 55–67 in Chinese with English abstract.
Sun, M., Yuan, C., Xiao, W., Long, X., Xia, X., Zhao, G., Lin, S., Wu, F., Kröner, A., 2008. Zircon U-Pb and Hf isotopic study of gneissic rocks from the Chinese Altai: progressive accretionary history in the early to middle Palaeozoic. Chem. Geol. 247, 352–383.
Tapponnier, P., Molnar, P., 1979. Active faulting and Cenozoic tectonics of the Tien Shan, Mongolia, and baykal regions. Journal of Geophysical Research-Solid Earth 84, 3425–3459.
Thébault, E., Purucker, M., Whaler, K.A., Langlais, B., Sabaka, T.J., 2010. The magnetic field of the earth's lithosphere. Space Sci. Rev. 155, 95–127.
Wang, B., Shu, L., Cluzel, D., Faure, M., Charvet, J., 2007. Geochemical constraints on Carboniferous volcanic rocks of the Yili Block (Xinjiang, NW China): implication for the tectonic evolution of Western Tianshan. J. Asian Earth Sci. 29, 148–159.
Wang, H., 1986. Precambrian geochronologic and chronostratigraphic subdivision of China. Earth Sci.-J. Wuhan College of Geol. 11 (5), 447–453 in Chinese with English abstract.
Wang, W., Pan, Y., Qiu, Z., 2009. A new edge recognition technology based on the normalized vertical derivative of the total horizontal derivative for potential field data. Appl. Geophys. 6 (3), 226–233.
Wang, W., Zhang, G., Liang, J., 2010. Spatial variation law of vertical derivative zero points for potential field data. Appl. Geophysic 7 (3), 197–209.
Wang, T., Tong, Y., Zhang, L., Li, S., Huang, H., Zhang, J., Guo, L., Yang, Q., Hong, D., Donskaya, T., Gladkochub, D., Tserendash, N., 2017. Phanerozoic granitoids in the central and eastern parts of Central Asia and their tectonic significance. Journal of Asian Earth Sciences 145(B):368-392. https://doi.org/10.1016/j.jseaes.2017.06.029.
Wang, T., Huang, H., Song, P., Wu, H., Zhang, J., Tong, Y., Du, K., Qin, Q., 2020. Studies of crustal growth and deep lithospheric architecture and new issues: exemplified by the Central Asian Orogenic Belt (Northern Xinjiang). Earth Sci. 45 (7), 2326–2344 in Chinese with English abstract.
Wang, Y., Han, G., Jiang, M., Yuan, X., 2004. Crustal structure along the geosciences transect from Altay to Altun Tagh. Chin. J. Geophys. 47 (2), 240–249 in Chinese with English abstract.
Windley, B.F., Allen, M.B., Zhang, C., Zhao, Z.Y., Wang, G.R., 1990. Paleozoic accretion and Cenozoic redeformation of the Chinese Tien Shan range, central Asia. Geology 18, 128–131.
Windley, B.F., Alexeiev, D., Xiao, W., Kröner, A., Badarch, G., 2007. Tectonic models for accretion of the Central Asian orogenic belt. Journal of the Geological Socity 164, 31–47.
Wu, Q., 1986. Structural evolution and prospects of Junggar Basin. Xinjiang Geology 4 (3), 1–10 in Chinese with English abstract.
Wu, S., Huang, R., Xu, Y., Yang, Y., Jiang, X., Zhu, L., 2018. Seismological evidence for a remnant oceanic slab in the western Junggar, Northwest China. J. Geophys. Res. Solid Earth 123, 4157–4170. https://doi.org/10.1029/2017JB015332.
Xiao, W., Han, C., Yuan, C., Sun, M., Lin, S., Chen, H., Li, Z., Li, J., Sun, S., 2008. Middle Cambrian to Permian subduction–related accretionary orogenesis of northern Xinjiang, NW China: Implications for the tectonic evolution of Central Asia. J. Asian Earth Sci. 32 (2–4), 102–117. https://doi.org/10.1016/j.jseaes.2007.10.008.
Xiao, W., Huang, B., Han, C., Sun, S., Li, J., 2010. A review of the western part of the Altaids: A key to understanding the architecture of accretionary orogens. Gondwana Res. 18, 253–273.
Xiao, W., Kusky, T., Safonova, I., Seltmann, R., Sun, M., 2015a. Tectonics of the Central Asian Orogenic Belt and its Pacific analogues. J. Asian Earth Sci. 113 (1), 1–6. https://doi.org/10.1016/j.jseaes.2015.06.032.
Xiao, W., Windley, B.F., Sun, S., Li, J., Huang, B., Han, C., Yuan, C., Sun, M., Chen, H., 2015b. A Tale of Amalgamation of Three Permo-Triassic Collage Systems in Central Asia: Oroclines, Sutures, and Terminal Accretion. Annu. Rev. Earth Planet. Sci. 43, 477–507.
Xiao, W., Shu, L., Gao, J., Xiong, X., Wang, J., Guo, Z., Li, J., Sun, M., 2009. Continental dynamics and mineralization in the Central Asian Orogenic Belt. Basic Sci. China-Research Progress 14–19 in Chinese with English abstract.
Xiao, W., Santosh, M., 2014. The western Central Asian Orogenic Belt: A window to accretionary orogenesis and continental growth. Gondwana Res. 25, 1429–1444.
Xiao, W., Windley, B.F., Han, C., Liu, W., Wan, B., Zhang, J., Ao, S., Zhang, Z., Song, D., 2018. Late Paleozoic to early Triassic multiple roll-back and oroclinal bending of the Mongolia collage in Central Asia. Earth Sci. Rev. 186, 94–128.
Xiao, W., Song, D., Windley, B., Li, J., Han, C., Wan, B., Zhang, J., Ao, S., Zhang, Z., 2019. Research progresses of the accretionary processes and metallogenesis of the Central Asian Orogenic Belt. Science China: Earth Sciences 49, 1512–1545 in Chinese with English abstract.
Xiao, X., Tang, Y., Wang, J., Gao, J., Zhao, M., 1994. Bluechist belts and their tectonic implications of the S. Tianshan Mts., N.W. China. Acta Geoscientia Sinica 3–4, 54–64 in Chinese with English abstract.
Xiao, W., Windley, B.F., Mark, B., Allen, M., Han, C., 2013. Paleozoic multiple accretionary and collisional tectonics of the Chinese Tianshan orogenic collage. Gondwana Res. 23, 1316–1341.
Xu, X., He, G., Li, H., Ding, T., Liu, X., Mei, S., 2006. Basic characteristics of the Karamay ophiolitic mélange, Xinjiang, and its zircon SHRIMP dating. Geology in China 33, 470–1086 in Chinese with English abstract.
Xu, Y., Yang, B., Zhang, S., Liu, Y., Zhu, L., Huang, R., Chen, C., Li, Y., Luo, Y., 2016. Magnetotelluric imaging of a fossil paleozoic intraoceanic subduction zone in western Junggar, NW China. J. Geophys. Res. Solid Earth 121, 4103–4117. https://doi.org/10.1002/2015JB012394.
Xu, Y., Yang, B., Zhang, A., Wu, S., Zhu, L., Yang, Y., Wang, Q., Xia, Q., 2020. Magnetotelluric imaging of a fossil oceanic plate in northwestern Xinjiang, China. Geology 48, 385–389. https://doi.org/10.1130/G47053.1.
Yang, G., Li, Y., Gu, P., Yang, B., Tong, L., Zhang, H., 2012. Geochronological and geochemical study of the Darbut Ophiolitic Complex in the west Junggar (NW China): Implications for petrogenesis and tectonic evolution. Gondwana Res. 21 (4), 1037–1049. https://doi.org/10.1016/j.gr.2011.07.029.
Yang, W., Zhang, L., Xu, Y., Yu, C., Yu, P., Zhang, B., Yang, B., 2015a. Three dimensional electrical resistivity structures of the Tarim Basin. Acta Geological Sinica 89 (12), 2203–2212 in Chinese with English abstract.
Yang, W., Zhang, L., Xu, Y., Yu, C., Yu, P., Zhang, B., Yang, B., 2015b. Magnetotellruic investigation and 3D lithospheric structures in the Tarim terrane. Acta Geological Sinica 89 (7), 1151–1161 in Chinese with English abstract.

Yang, X., Tian, X., Windley, B.F., Zhao, L., Lu, Y., Yuan, H., Xiao, W., 2022. The role of multiple trapped oceanic basins in continental growth: seismic evidence from the southern Altaids. Geophys. Res. Lett. 49 e2022GL098548.

Yu, X., Wang, Z., Zhou, X., Xiao, W., Yang, X., 2016. Zircon U-Pb geochronology and Sr-Nd isotopes of volcanic rocks from the Dahalajunshan Formation: Implications for Late Devonian-Middle carboniferous tectonic evolution of the Chinese Western Tianshan. Int. J. Earth Sci. 105 (5), 1637–1661. https://doi.org/10.1007/s00531-015-1275-y.

Zhang, C., Huang, X., 1992. The age and tectonic settings of ophiolites in west Junggar, Xinjiang. Geology Reviews 38, 509–523 in Chinese with English abstract.

Zhang, J., Xiao, W., Han, C., Mao, C., Chong, M., 2011. A Devonian to Carboniferous intra-oceanic subduction system in Western Junggar, NW China. Lithos 125, 592–606.

Zhang, J., Xiao, W., Han, C., Chao, Y., Min, S., Geng, H., Zhao, G., Guo, Q., Chong, M., 2012. Kinematics and age constraints of deformation in a Late Carboniferous accretionary complex in Western Junggar, NW China. Gondwana Res. 19, 958–974.

Zhang, J., Chen, Y., Xiao, W., Wakabayashi, J., Windley, B.F., Yin, J., 2021. Sub-parallel ridge-trench interaction and an alternative model for the Silurian-Devonian archipelago in estern Junggar and North-Central Tianshan in NW China. Earth Sci. Rev. 217, 103648.

Zheng, Q., Xu, X., Zhang, W., Zheng, Y., Liu, Y., Kuang, X., Zhou, D., Yu, X., Wang, B., 2021. A fossil Paleozoic subduction-dominated tranch-arc-basin system revealed by airborne magnetic-gravity imaging in West Junggar, NW China. Front. Earth Sci. 9, 760305.

Zhao, J., Li, Z., Cheng, H., Yao, C., Li, Y., 2004. Structure of lithospheric density and geomagnetism beneath the Tianshan orogenic belt and their geodynamic implications. Chin. J. Geophys. 47 (6), 1061–1067 in Chinese with English abstract.

Zhao, Y., Wang, R., Zhang, Y., Wang, X., Li, Z., Liang, H., 2011. Strike-slip structures and oil-gas exploration in the NW margin of the Junggar Basin. China. Acta Petrolei Sinica 32 (6), 976–984.

Zhu, X., Lu, M., 2016. Regional metallogenic structure based on aeromagnetic data in northern Chile. Appl. Geophys. 13 (4), 721–735.

Zhu, X., Lu, M., 2021. Fault structures and magmatic intrusions inferred from magnetic data for the Southern Great Xing'an Range. Northern China. Ore Geology Reviews 135, 104206.

Zhu, X., Lu, M., Guan, Y., Zhang, Y., 2018. Experiment on revealing the regional metallogenic structure based on the aeromagnetic data in the southern Da Hinggan Mountains. Geol. Bull. China 37 (2/3), 299–313 in Chinese with English abstract.

Zhu, X., Zheng, H., Lu, M., 2019. Lateral variation of aeromagnetic anomaly in South China and its tectonic implications. Int. J. Earth Sci. 108 (5), 1493–1507.

Zhu, X., Wang, L., Zhou, X., 2022. Structural features of the Jiangshao Fault Zone inferred from aeromagnetic data for South China and the East China Sea. Tectonophysics 826, 229252. https://doi.org/10.1016/j.tecto.2022.229252.

Zonenshain, L.P., Kuzmin, M.I., Natapov, L.M., 1990. Geology of the USSR: a plate-tectonic synthesis. In: Page, B.M. (Ed.), American Geophysical Union, Geodynam Series, 21. American Geophysical Union, Washington, DC, pp. 1–242.